Computational model for nanocarrier binding to endothelium validated using in vivo, in vitro, and atomic force microscopy experiments

Jin Liu[a], Gregory E. R. Weller[b], Blaine Zern[c,d], Portonovo S. Ayyaswamy[e], David M. Eckmann[a,b], Vladimir R. Muzykantov[c,d], and Ravi Radhakrishnan[a,1]

[a]Department of Bioengineering, [b]Department of Anesthesiology and Critical Care, [c]Institute for Environmental Medicine, [d]Department of Pharmacology, and [e]Department of Mechanical Engineering and Applied Mechanics, University of Pennsylvania, Philadelphia, PA, 19104

Edited by Barry H. Honig, Columbia University/HHMI, New York, NY, and approved August 3, 2010 (received for review May 18, 2010)

A computational methodology based on Metropolis Monte Carlo (MC) and the weighted histogram analysis method (WHAM) has been developed to calculate the absolute binding free energy between functionalized nanocarriers (NC) and endothelial cell (EC) surfaces. The calculated NC binding free energy landscapes yield binding affinities that agree quantitatively when directly compared against analogous measurements of specific antibody-coated NCs (100 nm in diameter) to intracellular adhesion molecule-1 (ICAM-1) expressing EC surface in in vitro cell-culture experiments. The effect of antibody surface coverage (σ_s) of NC on binding simulations reveals a threshold σ_s value below which the NC binding affinities reduce drastically and drop lower than that of single anti-ICAM-1 molecule to ICAM-1. The model suggests that the dominant effect of changing σ_s around the threshold is through a change in multivalent interactions; however, the loss in translational and rotational entropies are also important. Consideration of shear flow and glycocalyx does not alter the computed threshold of antibody surface coverage. The computed trend describing the effect of σ_s on NC binding agrees remarkably well with experimental results of in vivo targeting of the anti-ICAM-1 coated NCs to pulmonary endothelium in mice. Model results are further validated through close agreement between computed NC rupture-force distribution and measured values in atomic force microscopy (AFM) experiments. The three-way quantitative agreement with AFM, in vitro (cell-culture), and in vivo experiments establishes the mechanical, thermodynamic, and physiological consistency of our model. Hence, our computational protocol represents a quantitative and predictive approach for model-driven design and optimization of functionalized nanocarriers in targeted vascular drug delivery.

absolute binding free energy | Monte Carlo | targeted drug delivery | multivalent interactions | antibody surface coverage

Targeted delivery of functionalized nanocarriers (i.e., NCs coated with specific targeting ligands) to endothelium remains an important design challenge in pharmacological and biomedical sciences. The use of functionalized NCs offers a wide range of targeting options through tunable design parameters (size, shape, type, method of functionalization, etc.). This necessitates a multiparameter optimization for achieving efficacious targeting in drug delivery applications (1) including vascular-targeting in oncology (2–4).

Rational design of functionalized NCs faces many challenges owing to the complexities of molecular and geometric parameters surrounding receptor–ligand interactions and NCs (5–9), lack of accurate characterization of hydrodynamic, physico-chemical barriers for NC uptake/arrest (10–14), and uncertainty in targeting environment in vivo (15–17).

Among the factors impacting the design of NCs and therapeutic agents are: (*i*) binding affinity (18); (*ii*) multivalency or the average number of receptor–ligand bonds per bound NC (19–23); and (*iii*) in vivo targeting, measured as percentage of injected dose accumulated after intravenous injection (18).

Recently the binding affinity of functionalized NCs to ICAM-1 expressing EC surface has been studied experimentally. Muro et al. (18) reported that the binding association constant (K_a) of anti-ICAM-1 coated NC to EC can be two orders of magnitude higher than that of anti-ICAM-1 binding to ICAM-1. Haun and Hammer (24) investigated the kinetic rate constants of attachment and detachment of 210 nm NCs as a function of receptor density, ligand density on surface, and flow shear rate and identified a time dependence of the detachment rate due to multivalent binding. Ho et al. (25) studied the effect of antibody surface coverage (σ_s) on equilibrium binding constants by measuring fractional coverage of bound NCs (80 nm in diameter) as a function of NC concentrations; by fitting their experimental data, they observed linear dependence of K_a on σ_s, leading them to conclude that the system was dominated by monovalent interactions. Despite such previous studies on NC binding, a comprehensive understanding of the determinants of NC binding to EC in vitro and in vivo is lacking; this hampers rational design.

Computational determination of the binding affinities is a significant challenge because it involves the calculation of absolute binding free energies. This requires extensive sampling over conformational space and determination of various (translational and rotational) entropy changes upon binding. Using atomistic models, Woo and Roux (26) developed a general methodology to calculate K_a between a flexible ligand and a receptor based on the potential of mean force (PMF). Following the framework in ref. 26, here we develop a model to calculate the binding affinity of spherical NC functionalized with anti-ICAM-1 antibody to ICAM-1 expressing EC surface. Using a Monte Carlo approach, we compute the PMF profiles between NC and the EC surface and determine the absolute binding affinities. The important advantage of this protocol is that it allows us to systematically investigate the effects of a wide range of experimentally tunable parameters, including the receptor surface density, antibody coverage on NC (σ_s), flexural rigidity of the receptors, presence of glycocalyx, and effect of shear flow. We show that our model predictions can quantitatively describe the results of three broad classes of experiments, namely: (*i*) binding measurements of NCs in cell culture, (*ii*) in vivo targeting of NC to lung EC in mice, and (*iii*) biophysical characterization of NC–EC interaction using atomic force microscopy (AFM). For all cases investigated,

Author contributions: J.L., P.S.A., D.M.E., V.R.M., and R.R. designed research; J.L., G.E.R.W., B.Z., D.M.E., V.R.M., and R.R. performed research; J.L., B.Z., D.M.E., V.R.M., and R.R. analyzed data; J.L., D.M.E., V.R.M., and R.R. contributed new reagents/analytic tools; and J.L., P.S.A., D.M.E., and R.R. wrote the paper.

The authors declare no conflict of interest.

This article is a PNAS Direct Submission.

[1]To whom correspondence should be addressed. E-mail: rradhak@seas.upenn.edu.

This article contains supporting information online at www.pnas.org/lookup/suppl/doi:10.1073/pnas.1006611107/-/DCSupplemental.

model predictions agree remarkably well with experimental observations. Our results, thus, provide quantitative mechanistic understanding as well as help establish guiding principles for rational design of NC for efficacious EC targeting under various in vitro (cell-culture) and in vivo conditions.

Model

Model Parameters and MC Simulations. The NC is modeled as a rigid sphere (100 nm in diameter), and both the ligands and receptors are modeled as cylinders with reactive tips. The NC is constructed by uniformly distributing N_{ab} antibodies (anti ICAM-1) onto its surface (see Fig. 1). To make direct contact with the experimental system (18), the receptor parameters are chosen to mimic ICAM-1. The model parameters are summarized in Table S1.

The ligand parameters are chosen to mimic the murine anti-ICAM-1 antibody, which binds specifically to ICAM-1. The Bell model (27) provides the interactions between antibody and ICAM-1 through the reaction free energy: $\Delta G_r(d) = \Delta G_0 + \frac{1}{2}kd^2$, where d represents the distance between the reaction sites of the interacting antibody and ICAM-1, ΔG_0 is the free energy change at equilibrium state ($d = 0$) and k is the interaction bond force constant. Muro et al. (18) reported the equilibrium free energy change between antibody and ICAM-1 to be -7.98×10^{-20} J at 4 °C, which we set as ΔG_0 in our simulations. We obtain the bond spring constant $k = 1{,}000$ dyn/cm by fitting rupture-force distribution data reported from single-molecule force spectroscopy (28, 29). Both ΔG_0 and k are assumed to be temperature-independent based on which we derive the value of the reactive compliance γ (distance along the reaction coordinate to reach the transition state or point of rupture) to be ~0.4 nm, which agrees very well with experimental evaluations (29, 30). We also account for the ICAM-1 flexure (Fig. 1). Because the exact flexural rigidity for ICAM-1 proteins is not available in the literature, we set the flexural rigidity 7,000 pN·nm^2, which lies between glyco-proteins (700 pN·nm^2) and the actin filament (15–73×10^3 pN·nm^2) (10). An orientational bias MC sampling technique (31) is employed to explore the configurations of flexural movement while regular Metropolis Monte Carlo steps are employed for: (*i*) bond formation/breaking, (*ii*) NC translation and rotation, and (*iii*) ICAM-1 translation. Move i is selected randomly with a probability of 50%, and in the remaining 50%, the NC translation, rotation, and ICAM-1 translation are selected randomly with probability of $0.5 * N_{ab}/N_t$, $0.5 * N_{ab}/N_t$, and $(N_t - N_{ab})/N_t$ respectively; N_t is the combined total number of antibodies (N_{ab}) and ICAM-1 molecules. The simulations are run in parallel on four processors with different realizations of the same physical system. The error bars are reported as the standard deviation across multiple (four) realizations. An adaptive step size for NC translation/rotation and ICAM-1 diffusion is implemented to ensure a Metropolis acceptance rate of 50%.

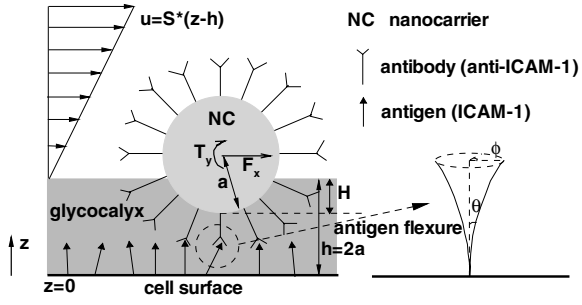

Fig. 1. Schematic of the NC adhesion model. The adhesion is mediated through interactions between anti-ICAM-1 antibody on NC (radius a = 50 nm) and ICAM-1s on EC surface. The ICAM-1 flexure is taken into account by allowing it to bend and rotate in θ and ϕ, a steady shear flow with shear rate of S as well as glycocalyx with height of $h = 2a$ are introduced.

Absolute Binding Free Energy. For binding of ligands (**L**) (or NC) to receptors (**R**), the binding process can be described as: $\mathbf{L} + \mathbf{R} \rightleftharpoons \mathbf{LR}$, where **LR** is the ligand and receptor in binding state. At thermodynamic equilibrium, the binding affinity (or association constant) K_a is defined as:

$$K_a = \frac{[\mathbf{LR}]}{[\mathbf{L}][\mathbf{R}]} = \frac{p_1[\mathbf{R}]_{\text{tot}}}{[\mathbf{L}]p_0[\mathbf{R}]_{\text{tot}}} = \frac{1}{[\mathbf{L}]} \times \frac{p_1}{p_0}. \quad [1]$$

Here [**L**], [**R**], and [**LR**] are concentrations of each species. We define p_0 and p_1 as the fraction of receptors with no ligand and one ligand bound respectively, so that [**R**] and [**LR**] can be expressed as $[\mathbf{R}] = p_0[\mathbf{R}]_{\text{tot}}$ and $[\mathbf{LR}] = p_1[\mathbf{R}]_{\text{tot}}$, where $[\mathbf{R}]_{\text{tot}}$ is the total receptor concentration in the whole system. We relate the fraction in Eq. **1** to the ratio of the integral of configurational degrees of freedoms in the bound state to the unbound state (26):

$$K_a = \frac{1}{[\mathbf{L}]} \times \frac{\int_{\text{bound}} d\mathbf{1}d\mathbf{X}e^{-\beta U_{\text{bound}}}}{\int_{\text{unbound}} d\mathbf{1}d\mathbf{X}e^{-\beta U_{\text{unbound}}}}, \quad [2]$$

where U_{bound} and U_{unbound} are the total potential energies of the system at bound and unbound states, $\beta = 1/k_{\text{B}}T$ in which k_{B} is the Boltzmann constant and T is the absolute temperature. **1** represents all the degrees of freedom associated with the ligand (NC) and **X** is the degrees of freedom for the remaining molecules (receptors). On a per ligand basis, the ligand concentration is $[\mathbf{L}] = 1/V_{\text{unbound}}$, where the denominator is the volume accessible to an unbound ligand. The integral associated with the unbound state ($U_{\text{unbound}} = 0$) in Eq. **2** is determined over translational degrees of freedom (yielding the volume V_{unbound}), and rotational degrees of freedom (yielding a factor of $8\pi^2$ in three dimensions).

We choose a reaction coordinate z along which we perform umbrella sampling with harmonic biasing potentials. The umbrella sampling is performed with window size of $\Delta z = 0.05$ nm, and the harmonic biasing potential in each window is chosen to be $0.5k_u(z - z_{0,i})^2$, where $0.5k_u(\Delta z)^2 = 1.0 \times 10^{-20}$ J, k_u is the harmonic force constant and $z_{0,i}$ is the location of the center of window i. The NC is slowly moved to the cell surface by updating $z_{0,i}$. A total of 200 million Monte Carlo steps are performed in each window, and the histogram is stored only when there exists at least one bond. All the relevant parameters including the window size Δz, strength of the biasing potential k_u, and the sampling size in each window have been tested to ensure convergence. The weighted histogram analysis method (WHAM) algorithm (32) is used to unbias and combine the histograms in different windows to form a complete PMF ($W(z)$) profile using a tolerance factor of 10^{-6}. PMF profiles for each system are averaged over four independent realizations and the standard deviation is reported as the error bar.

Binding of Antibody-Coated NC to EC Surface. In calculating K_a for antibody-coated NC using a Langmuir model framework (see section S2 in *SI Text*), we first compute the PMF ($W(z)$) profiles of NC binding to receptors expressed on a minimal patch on the EC surface, which allows firm binding; here the reaction coordinate z is defined as the vertical distance between the center of NC and the EC surface. The binding association constant is calculated as:

$$K_a = \frac{1}{[\mathbf{L}]} \times T_1 \times T_2 \times T_3. \quad [3]$$

Three terms T_1–T_3 account for entropy loss upon binding: T_1 accounts for the entropy loss of receptors associated with binding to the minimal patch:

$$T_1 = \frac{A_{R,b}^{(1)} \times A_{R,b}^{(2)} \times \ldots \times A_{R,b}^{(N_b)}}{A_{R,ub}^{(1)} \times A_{R,ub}^{(2)} \times \ldots \times A_{R,ub}^{(N_b)}}, \quad [4]$$

where $A_{R,b}^{(n)}$ is the accessible surface area of the nth bound receptor in its bound state and $A_{R,ub}^{(n)}$ is the accessible surface area of the nth receptor in its unbound state. T_2 is associated with the NC rotational entropy loss in binding, and T_3 is related to loss of NC translational entropy:

$$T_2 = \frac{(N_{ab}/N_b)\Delta\omega}{8\pi^2}; \qquad T_3 = \frac{A_{NC,b}\int e^{-\beta W(z)}dz}{A_{NC,ub}l_z}, \quad [5]$$

where N_b is the total number of bonds in equilibrium state. $\Delta\omega$ is the rotational volume of the NC in the bound state which is quantified using the rmsd of Euler angles (see section S3 in *SI Text*) (33). $A_{NC,b}$ is the accessible area to the NC in the bound state, $A_{NC,ub}$ and $A_{NC,ub}l_z$ are the area and volume accessible to the NC in the unbound state, and $W(z)$ is the calculated PMF profile. T_1–T_3 and $W(z)$ are computed from our simulations (see *Results*). Substitution of the NC concentration $[\mathbf{L}] = 1/(A_{NC,ub}l_z)$ in Eq. **3** yields the final expression of the binding constant K_a.

Results

Binding of NC to EC Surface. We initially set $N_{ab} = 162$, which corresponds to 74% of saturation coverage (see *Materials and Methods*). The computed PMF (Fig. 2*A*) at $T = 27$ °C indicates three firm bonds on average (multivalency or $N_b = 3$) characterized by a PMF well of $32k_BT$ when projected along z. The PMF change is smaller for the second and third bonds compared to the first as a result of ICAM-1 flexure and differences in loss in translational and rotational entropies of NC as well as ICAM-1. The multivalency or the number of bonds formed at equilibrium is affected by the bond reaction free energy, bond spring constant, ICAM-1 bending rigidity, antibody surface coverage (Fig. S5), and NC size (Figs. S3 and S4). Fig. 2*B* also shows the projection (on the xy plane) of the spatially averaged distribution of bound ICAM-1 relative to the center of NC. The outer envelope of the bond distribution in *B* defines the minimal patch on the EC surface for compete NC binding; the first bound ICAM-1 can freely access the area within the outer circle with outer radius $r_o = 12.5$ nm (see section S2 of *SI Text*), yielding $A_{R,b}^{(1)} = \pi r_o^2$, the second bound ICAM-1 can only access the area within the annulus between the outer and inner circles (inner radius $r_i = 9.7$ nm) with corresponding $A_{R,b}^{(2)} = \pi(r_o^2 - r_i^2)$, and the third bound ICAM-1 is restricted to a patch with accessible area $A_{R,b}^{(3)} = (r_o - r_i)^2$. In contrast, each of these ICAM-1 molecules in the unbound state can access a surface area of πr_o^2. Similarly, the translational area accessed by a bound NC is $A_{NC,b} = (r_o - r_i)^2$, and as stated above the rotational mobility of bound NC $\Delta\omega$ is estimated from the rmsd of Euler angle fluctuations in the bound state, (see section S3 of *SI Text* and Fig. S2). Substitution into Eq. **3** yields the expression:

$$K_a = \frac{(N_{ab}/3)\Delta\omega}{8\pi^2} \times \frac{\pi(r_o^2 - r_i^2)(r_o - r_i)^4 \int e^{-\beta W(z)}dz}{(\pi r_o^2)^2}. \quad [6]$$

Based on the calculated PMF in Fig. 2, the computed binding association constant $K_a = 5.9 \times 10^{10}$ nm^3 and the dissociation constant $K_d = 1/K_a = 28.0$ pM, which compares very favorably with the in vitro measurement of 77 pM under similar conditions at a temperature of 4 °C (18) (see section S2 of *SI Text* and Fig. S1).

Effect of Antibody Surface Coverage. The antibody surface coverage on NC (σ_s) is a tunable experimental parameter shown to influence NC binding in vitro (34). To study the effect of σ_s, we carried out simulations with antibody surface coverages $N_{ab} = 12$, 42, 60, 75, 100, 140, and 162 per NC (i.e., $\sigma_s \sim 5$–74% of saturation coverage). The computed PMF profiles and corresponding bond distributions are provided in section S6 of *SI Text* and Fig. S5, and the corresponding binding association constant as a function of antibody coverage is provided in Fig. 3*A*.

From Eq. **5**, σ_s impacts the NC binding constant in two ways: (*i*) the multiplicity factor N_{ab}/N_b is a geometric effect and defines a linear dependence of K_a on σ_s when the multivalency is unaltered; (*ii*) the more significant effect results from changes in the calculated PMF profiles due to changes in multivalency, which exponentially affects K_a, (through the exponential integration term in Eq. **5**). In Fig. 3*A*, the linear dependence is verified (see dotted lines) for the two ranges of σ_s, which support constant multivalency. Below a threshold value of $\sigma_s \sim 45\%$, there is an exponential decrease in K_a where the PMF drops by $\sim 8k_BT$ as the average multivalency decreases from three to two. Significantly, for $\sigma_s < 45\%$, the K_a of NC is lower than that of free antibody binding to ICAM-1 (see dash-dot blue line). The primary reason for the decrease of K_a for NC below that of free ICAM-1-antibody value is that the rotational entropy loss of the NC (Eq. **5**) is much greater than that for the free ICAM-1-antibody binding. Further discussion on the regime $\sigma_s \ll 1$ is provided in section S5 of *SI Text*.

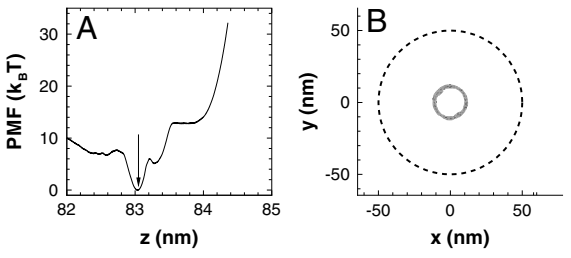

Fig. 2. (*A*) Calculated PMF $W(z)$ as function of distance between center of NC and cell surface. (*B*) The averaged spatial distribution antibody-ICAM-1 bound pairs at equilibrium state indicated by the arrow in *A* projected on the EC surface (xy plane). The antibody surface density is $\sigma_s = 162$/NC, which corresponds to 74% of saturation coverage. The dotted circle represents the projection of NC boundary on the EC surface, provided as a reference.

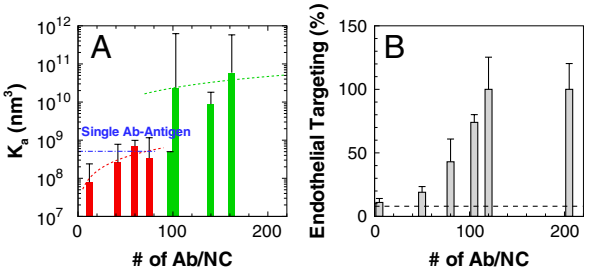

Fig. 3. The computed binding association constant K_a as a function of antibody surface coverage σ_s (*A*). The dotted lines represent linear dependence of σ_s, the blue dash-dot line indicates the binding affinity of single antibody to ICAM-1. The error bars are calculated from four independent realizations. In calculating the PMF of NC at $\sigma_s = 45\%$, three out of the four realizations yielded an average multivalency of three, while the other realization yielded an average multivalency of two; hence the K_a values are computed and plotted separately for the two cases. This dependence of multivalency on the spatial distribution of the antibodies on NC suggests that, owing to the heterogeneity, the experiments will show a continuous increase in K_a over a narrow range of σ_s, rather than a discontinuity at the threshold σ_s value. (*B*) In vivo endothelium targeting of NCs with varying surface coverage with anti-ICAM-1 molecules in mice. The dotted line is the plot of IgG coated NC and provides a background for nonspecific ICAM targeting.

Effect of Hydrodynamic Shear and Glycocalyx. To evaluate the role of hydrodynamic force, as displayed in Fig. 1, a steady shear flow with a shear rate S is considered. The force and torque exerted on the NC (F_x and T_y in Fig. 1) are computed by solving the Stokes equation. The effect of shear on the specific binding of NC is investigated by comparing the equilibrium distributions of multivalency in the presence and absence of shear for a range of σ_s values (see section S7 of *SI Text* and Fig. S6). Even though the magnitude of the shear force on the 100 nm NC is small (the energy change of the NC due to the shear gradient is 2% of k_BT), shear flow does quantifiably perturb the distribution of multivalency (Fig. S6) and introduces a slight asymmetry in the distribution of flexure angles. This effect is small, and the flow-field is not expected to alter the adhesion landscape nor the computed binding affinity (which were both computed under zero shear) except for the low antibody coverage ($\sigma_s \leq 14\%$). In this case, as evident from the low σ_s cases in Fig. S6, the population of states with multivalency less than two under shear is increased, which implies that a shear induced detachment of the NC is likely.

We account for the glycocalyx by introducing a layer of $h = 100$ nm in height above the cell surface. In ref. 10, the flow in the glycocalyx layer is described using the Brinkman equation. Here, we only consider the effect of glycocalyx in the absence of flow by considering the normal resistance through a harmonic potential $1/2k_{glyx}H^2$ per unit differential area of the NC surface immersed in the glycocalyx; H is the penetration depth of the NC into glycocalyx (see Fig. 1) and k_{glyx} is the glycocalyx stiffness. We obtain k_{glyx} by fitting in vivo experimental data (15). This enables us to compute a difference in free energy of binding in the presence and absence of glycocalyx: $\Delta E_{glyx} = \frac{1}{3}k_{glyx}\pi a^4 \sim 6k_BT$, when the NC is fully immersed in the glycocalyx (28). The effect of the glycocalyx layer is to alter (lower) the PMF and decrease the binding affinity for all values of σ_s (see Fig. S7). Presence of the glycocalyx does not alter the effect of antibody surface coverage on the binding affinity but significantly decreases the fractional binding of NC for a given value of σ_s. Taken together, the data in Fig. 3 and Figs. S6 and S7 implies that for 100 nm NCs, the trends we have computed from equilibrium binding data in the absence of flow for characterizing the effect of σ_s may apply both to cell-culture experiments in moderate shear flow ($S \leq 6{,}000\ s^{-1}$), in vivo experiments, where the binding may occur in the presence of glycocalyx.

Comparison with in Vivo Experiments. For a direct comparison of the predicted K_a vs. σ_s, we quantified endothelial targeting as a function of lung uptake of NCs in mice. Lung uptake is representative of endothelial targeting because the lung accounts for roughly 30% of the endothelium in vivo (35). Moreover, additional data (see Fig. S8 and section S8 of *SI Text*) indicate that only uptake in the pulmonary vasculature is dependent on the number of anti-ICAM molecules; thus we do not account for nontargeted tissues, because the uptake of particles in the main reticuloendothelial system (RES) organ, liver, did not change with variations of the anti-ICAM surface density. Fig. 3*B* depicts endothelium targeting of NCs with varying surface coverage with anti-ICAM-1 molecules. Full coverage of NCs was expressed as 100% endothelium targeting because it corresponds to the highest localization to the lung. Most significantly, the predicted behavior of σ_s versus NC binding in Fig. 3*A* agrees remarkably well with in vivo results in Fig. 3*B*.

Comparison with AFM Experiments. To make a direct comparison of our computed PMF for NC binding with AFM force measurements probing the interactions of anti-ICAM-1 functionalized NC with EC surface, we computed the rupture-force distribution (36) of the attached NC at different loading rates (see section S9 in *SI Text*). The computed force distribution in Fig. 4*A*, based on our computed PMF profile for $\sigma_s = 74\%$, reveals a mean rupture force of 215–230 pN with a standard deviation of 40 pN at a loading rates of 100–200 nN/s.

The AFM experiments probing the interactions of the AFM tip functionalized with antibody-bearing NCs were carried out. A typical trace showing a single rupture event is shown in Fig. 4*B*; triplet events were also observed in some cases (see Fig. S9*A*). The complete distribution of experimental NC rupture forces (see inset) shows a mean rupture force of 316 pN with a standard deviation of 48 pN over 89 experiments. For comparison, AFM experiments for ICAM-1 immobilized surface with AFM tip directly functionalized with antibody (i.e., without NC) shows a rupture force of 291 pN and a standard deviation of 32 pN over 174 experiments (Fig. S9*B*). The model results in panel *A* compare favorably with experimentally determined rupture-force measurements in the inset of panel *B* (see section S9 of *SI Text* for a sensitivity analysis). As an additional check, we estimate the reactive compliance to be $\gamma \sim 0.2$ nm (see section S9 in *SI Text*), which closely agrees with results from single-molecule experiments (29, 30). Given that the rupture-force distribution is governed mainly by k rather than by ΔG_0 (see section S9 of *SI Text*), the agreement of model predictions with AFM measurements establishes a mechanical consistency of the model, which is independent of the thermodynamic consistency achieved from the close agreement of the computed binding affinity with that measured in binding experiments. We also note that the predicted multivalency of 3 evident from the PMF in Fig. 2 (for $\sigma_s = 74\%$) is consistent with some (5–10%) of the AFM force traces which record multiple rupture events (Fig. S9*A*).

Discussion

We present a general protocol to calculate the absolute binding affinity for specific binding of NC to functionalized surfaces mediated through receptor–ligand interactions. Our results for the binding affinities of 100 nm antibody-coated NCs at large surface coverage ($\sigma_s \geq 45\%$) to ICAM-1 expressing EC surface shows several hundredfold enhancement in binding compared

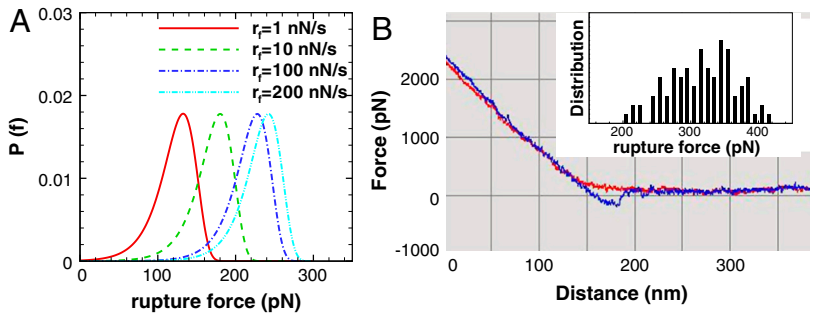

Fig. 4. (*A*) The calculated distribution of rupture forces at different loading rates. (*B*) Representative AFM experimental measurement of the force-displacement curve. The red tracing shows cantilever approach to sample surface, blue tracing shows withdrawal. The time-sampling is set at 12,000 s^{-1}. In the inset, the distribution of rupture forces from the multiple experiments are reported. The force loading rate in the experiment lies in the range 96–192 nN/s.

with that of isolated antibody to ICAM-1. This prediction agrees remarkably well with experimental measurements of the NC affinity to EC in cell culture (18), as depicted in Fig. S1. Our results on the computed effect of surface coverage of antibodies σ_s on NC binding suggests a linear effect of σ_s on K_a for $0 < \sigma_s < 45\%$ and for $\sim 45\% < \sigma_s \leq 100\%$; in these regimes, the average multivalency is not altered, and the linear effect arises from contributions of translational and rotational entropy losses upon NC binding (see red and green dotted lines in Fig. 3*A*). At the threshold of antibody coverage $\sigma_s \sim 45\%$ we predict an exponential effect of σ_s on K_a primarily due to a change in multivalency associated with NC binding (Figs. S5 and S6). We note that for $\sigma_s > 45\%$, the increase in NC binding affinity with increasing σ_s is only modest, while for $\sigma_s \lessapprox 45\%$, the NC binding affinity abruptly drops below that for free antibody with ICAM-1. Our results imply a negligible effect of shear ($S \leq 6{,}000\ s^{-1}$) when $\sigma_s \geq 14\%$ (see Fig. S6). Moreover, the glycocalyx while reducing the fractional binding at a given σ_s, does not alter the dependence of K_a on σ_s (see Fig. S7). We are therefore justified in comparing the model results with in vivo data of NC binding and targeting to mice endothelium. Most significantly, the model prediction of σ_s versus NC binding agrees remarkably well with in vivo results (see Fig. 3*B*), while simultaneously providing consistent agreement with AFM force-rupture experiments (Fig. 4) as well as in vitro equilibrium binding experiments (Fig. S1).

Our model is predictive for binding of spherical nanocarriers to endothelial apical molecules and defining the critical threshold of antibody density for effective anchoring as well as the associated multivalent interactions. The practical significance is that, exceeding the optimal surface density of antibody or other affinity ligands on the surface of nanocarriers may predispose to immune response to the protein. The model is designed to predict results for targeting to a well appreciated target (ICAM-1) and can be easily adapted to other endothelial molecules localized on the apical luminal surface of endothelium at similar density to ICAM-1 $\sim 10^5$ copies per cell (angiotensin-converting enzyme, VCAM-1, thrombomodulin, etc.). In the future, the model may also be extended further to treat distinct endothelial epitopes (such as molecules localized to the caveoli), filamentous carriers, or intracellular uptake of carriers. Despite their absence in the current model description, the remarkable agreement of the computed results with three broad and independent classes of experiments, namely, AFM rupture-force, in vitro binding affinity, and in vivo endothelial targeting in mice, strongly imply mechanical, thermodynamic, as well as physiological consistency. On these bases, our model represents a promising tool for the rational design of functionalized NCs in targeted drug delivery.

Materials and Methods

Preparation of NC. A solvent extraction emulsification procedure was used to form PLGA NCs whose size (100 nm) and zeta-potential were determined on a Brookhaven 90Plus zeta-potential and dynamic light scattering apparatus (18). Anti-ICAM-1 nanocarriers were prepared by coating green fluorescent polystyrene beads with antimurine ICAM-1 (18). Radiolabeled NCs were prepared containing a mix of anti-ICAM-1 and ^{125}I-IgG at 95:5 molar ratio. After separation of the free anti-ICAM-1 by centrifugation, the amount of ^{125}I tracer coated onto the nanocarriers was determined in a gamma counter. This procedure was employed to synthesize as well as characterize a range of surface coverages of antibodies on NC ($5\% < \sigma_s \leq 100\%$). The saturating antibody surface coverage on the NC surface was estimated to be 220 antibody molecules per NC (or 7,000 antibody per μm^2) (18, 34), which we assumed as 100% coverage. The diameter of the anti-ICAM-1 coated NCs was determined by dynamic light scattering to be 92 ± 6 nm.

In Vivo Targeting to Vascular Endothelium in Mice. Anesthetized C57BL/6 female mice (16–24 g, Harlan) were injected intravenously via jugular vein with NCs coated with murine anti-ICAM-1 (YN1 clone, Biolegend) or control rat IgG (Jackson Labs). The injected dose was ~200 μl (or ~10 mg/kg) with a tracer amount of antibody-coated ^{125}I-labeled NC. Blood was collected from the retro-orbital plexus at 30 min post-injection and organs (heart, kidneys, liver, spleen, and lungs) were collected at 30 min post-injection. Radioactivity and weight of the samples were determined to calculate NC targeting. These studies were carried out in accordance with the Guide for the Care and Use of Laboratory Animals as adopted and promulgated by the National Institutes of Health.

AFM Experiments. Silicon nitride AFM cantilevers were functionalized with maleimide-terminated flexible polyethylene glycol linkers (Novascan, Ames, IA) having a nominal spring constant of 0.06–0.12 N/m. These were incubated with antibody-coated 1 μm diameter polystyrene beads in phosphate-buffered saline (PBS) (18, 34) for 10 min, then washed three times to remove the excess. Recombinant human ICAM-1 (rhICAM; R&D Systems, Minneapolis) at a concentration of 25 μg/mL in PBS was adsorbed onto clean glass coverslips for 15 min, then washed three times to remove the excess.

An atomic force microscope (Molecular Imaging 5500, Tempe, AZ) was used in force spectroscopy mode to obtain force-distance cycles for functionalized cantilever-functionalized coverslip interactions at fixed velocities of 1.6 μm/s (corresponding to a force loading rate of 96–192 nN/s). Experiments were conducted in PBS at 20 °C. The negative control experiments (performed by blocking available ICAM-1 sites by incubating with excess free anti-ICAM-1 antibody) yielded no significant binding interaction between the cantilever and the sample surface.

ACKNOWLEDGMENTS. We thank N.J. Agrawal, U. Balakrishnan, T.N. Swaminathan, A. Calderon, and R. J. Composto for helpful discussions. This work was supported by National Institutes of Health Grants R01-EB006818 (D.M.E.) and R01-HL087036 (V.R.M.), National Science Foundation (NSF) Grant CBET-0853389 (R.R.), and NSF/NBIC at UPenn. Computational resources were provided in part by the National Partnership for Advanced Computational Infrastructure under Grant No. MCB060006.

1. Khademhosseini A, Langer R (2006) Nanobiotechnology—Drug delivery and tissue engineering. *Chem Eng Prog* 102:38–42.
2. Siemann DW (2006) *Vascular-targeted therapies in oncology* (John Wiley and Sons, Ltd., West Sussex, UK).
3. Arap W, Pasqualini R, Ruoslahti E (1998) Cancer treatment by targeted drug delivery to tumor vasculature in a mouse model. *Science* 279:377–380.
4. Allen TM, Cullis PR (2004) Drug delivery systems: Entering the mainstream. *Science* 303:1818–1822.
5. Champion JA, Mitragotri S (2006) Role of target geometry in phagocytosis. *Proc Natl Acad Sci USA* 103:4930–4934.
6. Champion JA, Katare YK, Mitragotri S (2007) Making polymeric micro- and nanoparticles of complex shapes. *Proc Natl Acad Sci USA* 104:11901–11904.
7. Champion JA, Walker A, Mitragotri S (2008) Role of particle size in phagocytosis of polymeric microspheres. *Pharm Res* 25:1815–1821.
8. Muro S, et al. (2008) Control of endothelial targeting and intracellular delivery of therapeutic enzymes by modulating the size and shape of ICAM-1-targeted carriers. *Mol Ther* 16:1450–1458.
9. Charoenphol P, Huang RB, Eniola-Adefeso O (2010) Potential role of size and hemodynamics in the efficacy of vascular-targeted spherical drug carriers. *Biomaterials* 31:1392–1402.
10. Weinbaum S, Zhang X, Han Y, Vink H, Cowin C (2003) Mechanotransduction and flow across the endothelial glycocalyx. *Proc Natl Acad Sci USA* 100:7988–7995.
11. Cedervall T, et al. (2007) Understanding the nanoparticle-protein corona using methods to quantify exchange rates and affinities of proteins for nanoparticles. *Proc Natl Acad Sci USA* 104:2050–2055.
12. Linse S, et al. (2007) Nucleation of protein fibrillation by nanoparticles. *Proc Natl Acad Sci USA* 104:8691–8696.
13. Lundqvist M, et al. (2008) Nanoparticle size and surface properties determine the protein corona with possible implications for biological impacts. *Proc Natl Acad Sci USA* 105:14265–14270.
14. Lynch I, Dawson KA (2008) Protein-nanoparticle interactions. *Nano Today* 3:40–47.
15. Mulivor AW, Lipowsky HH (2002) Role of glycocalyx in leukocyte-endothelial cell adhesion. *Am J Physiol Heart Circ Physiol* 283:H1282–H1291.
16. Damiano ER, Long DS, Smith ML (2004) Estimation of viscosity profiles using velocimetry data from parallel flows of linearly viscous fluids: application to microvascular haemodynamics. *J Fluid Mech* 512:1–19.
17. Smith ML, Long DS, Damiano ER, Ley K (2003) Near-wall μ-PIV reveals a hydrodynamically relevant endothelial surface layer in venules in vivo. *Biophys J* 85:637–645.
18. Muro S, et al. (2006) Endothelial targeting of high-affinity multivalent polymer nanocarriers directed to intercellular adhesion molecule 1. *J Pharmacol Exp Ther* 317:1161–1169.
19. Mourez M, et al. (2001) Designing a polyvalent inhibitor of anthrax toxin. *Nat Biotechnol* 19:958–961.
20. Rai P, et al. (2006) Statistical pattern matching facilitates the design of polyvalent inhibitors of anthrax and cholera toxins. *Nat Biotechnol* 24:582–586.
21. Basha S, et al. (2006) Polyvalent inhibitors of anthrax toxin that target host receptors. *Proc Natl Acad Sci USA* 103:13509–13513.
22. Vance D, Martin J, Patke S, Kane RS (2009) The design of polyvalent scaffolds for targeted delivery. *Adv Drug Deliver Rev* 61:931–939.

23. Kaittanis C, Santra S, Perez JM (2009) Role of nanoparticle valency in the nondestructive magnetic-relaxation-mediated detection and magnetic isolation of cells in comples media. *J Am Chem Soc* 131:12780–12791.
24. Haun JB, Hammer DA (2008) Quantifying nanoparticle adhesion mediated by specific molecular interactions. *Langmuir* 24:8821–8832.
25. Ho K, Lapitsky Y, Shi M, Shoichet MS (2009) Tunable immunonanoparticle binding to cancer cells: thermodynamic analysis of targeted drug delivery vehicles. *Soft Matter* 5:1074–1080.
26. Woo H, Roux B (2005) Calculation of absolute protein-ligand binding free energy from computer simulations. *Proc Natl Acad Sci USA* 102:6825–6830.
27. Bell GI, Dembo M, Bongrand P (1984) Competition between nonspecific repulsion and specific bonding. *Biophys J* 45:1051–1064.
28. Agrawal NJ, Radhakrishnan R (2007) Role of glycocalyx in mediating nanocarrier cell adhesion explored using a thermodynamic model and Monte Carlo simulation. *J Phys Chem C* 111:15848–15856.
29. Zhang X, Wojcikiewicz E, Moy VT (2002) Force spectroscopy of the leukocyte function-associated antigen-1/intercellular adhesion molecule-1 interaction. *Biophys J* 83:2270–2279.
30. Hanley W, et al. (2003) Single molecule characterization of P-selectin/ligand binding. *J Biol Chem* 278:10556–10561.
31. Frenkel D, Smit B (2001) *Understanding Molecular Simulation: From Algorithms to Applications* (Academic, Orlando, FL), pp 322–331.
32. Roux B (1995) The calculation of the potential of mean force using computer simulations. *Comput Phys Commun* 91:275–282.
33. Carlsson J, Åqvist J (2005) Absolute and relative entropies from computer simulation with applications to ligand binding. *J Phys Chem B* 109:6448–6456.
34. Calderon AJ, Muzykantov V, Muro S, Eckmann DM (2009) Flow dynamics, binding and detachment of spherical carriers targeted to ICAM-1 on endothelial cells. *Biorheology* 46:323–341.
35. Davies MG, Hagen PO (1993) The vascular endothelium. A new horizon. *Ann Surg* 218:593–609.
36. Evans E, Ritchie K (1997) Dynamic strength of molecular adhesion bonds. *Biophys J* 72:1541–1555.